23rd ABCM International Congress of Mechanical Engineering
December 6-11, 2015, Rio de Janeiro, RJ, Brazil

TURBULENT DRAG REDUCTION IN FLOWS PAST A FLAT PLATE WITH MICROGROOVES

Paulo Arthur Beck
Horácio Antonio Vielmo
Department of Mechanical Engineering, Federal University of Rio Grande do Sul (UFRGS), Rua Sarmento Leite 425, 90050-170, Porto Alegre, RS, Brazil
paulo.beck@ufrgs.br, vielmoh@mecanica.ufrgs.br

Abstract. *The potential in drag reduction of turbulent flows over a flat plate with streamwise aligned microgrooves is investigated. For this purpose, the connection between the anisotropy of the Reynolds stresses and the drag reduction effect is presented, and a model is developed in order to estimate the drag reduction potential according to flow and geometrical settings. The Navier-Stokes transport equations particularized for incompressible flows are used to describe the fluid motion, and the turbulence quantities are evaluated using the linear pressure-strain Reynolds stress transport model. The quantities are estimated using the Finite -Volume method, which is applied to a set of grids with different refinement levels. After validating the numerical method against the predictions of the proposed model, and the theoretical and DNS estimates available in the literature, the authors discuss the drag reducing effect by examining the state of turbulence in the microgrooves, also providing an assessment on the anisotropy of the Reynolds Stresses inside, near and outside the grooves.*

Keywords: *drag reduction, microgrooves, turbulence.*

1. INTRODUCTION

The research on turbulent drag reduction justifies as most flows of technological interest are turbulent, and drag plays a major role in energy consumption. Moreover, the increasingly restrictive environmental legislation pressures manufacturers, in particular those in the aeronautical industry, to deliver products embedding drag-reducing technologies. As an example, in the Flightpath 2050 Europe's Vision for Aviation report (European Commission, 2011) several goals are set to achieve in the year 2050 a 75% reduction in $\mathrm{CO_2}$ emissions per passenger-kilometer, and a 90% decrease in NO_x emissions, both relative to the capabilities of a typical new aircraft in the year 2000. In this prospect, the development of flow control methods with the purpose of saving energy and reducing emissions is a key area of research in fluid dynamics (Gollub, 2006).

Thiede (2001) categorizes the flow control methods as either active or passive, and in this work the authors focus their attention on microgrooves, a particular strategy within the scope of the latter category. Passive flow control methods attain the drag reduction effect by altering the state of turbulence in the near-wall region by means of topological modifications such as riblets and microgrooves. Several sources offer insight on the drag reduction effect of riblets and microgrooves. The experimental investigation of Hooshmand et al. (1983), and the numerical study of Choi et al. (1992) showed that the shear-stress is reduced in the region between riblets as a consequence of the thickening of the viscous sublayer. Choi (1989) showed that the kinematic constraint of the traverse velocity fluctuations causes the drag reduction effect. Walsh (1990) indicated that regions of low-speed fluid propagate in the streamwise direction, then oscillate and eventually detach off the surface. The Reynolds stresses generated during this bursting process, and the subsequent mixing represent most of the Reynolds stress production in the turbulent boundary layer. Therefore, microstructures capable to constrain near-wall motions cause the Reynolds stress production to decrease, and hence reduce the turbulent drag. Van Schwarz-Manen et al. (1990), and Suzuki and Kasagi (1994) explain the drag reduction effect as a consequence of the decay of the coherent structures in the near-wall region, as the flow slows down in the gap between microstructures. Bechert et al. (1997) explain the drag reduction as a consequence of the decrease of the turbulence dissipation rate caused by the microstructures constraining secondary flows and vortices, which in turn reduces the turbulent viscosity and ultimately the drag. In particular for microgrooves, the experimental results of Frohnapfel et al. (2007) showed that drag reduction is achieved when the state of turbulence of the small and large scales satisfies the condition of local axisymmetry under rotation around the axis that is aligned with the main flow direction, and Mohammadi and Floryan (2013) showed that properly structured grooves are able to eliminate the wall shear from the majority of the wetted surface area regardless of the groove orientation. Such findings side with the theoretical analysis in the literature (Jovanović and Hillerbrand, 2005; Jovanović et al., 2006) demonstrating that the local axisymmetry imposes kinematic restrictions that force the state of turbulence to become one-component near the wall, thus reducing the transport of momentum into the walls, and consequently the skin friction.

In this paper, the authors present a method that accomplishes such goal while demonstrating the drag-reducing effect in flows past a flat plate with streamwise microgrooves. For this purpose, a model is formulated to allow the estimation of the drag-reducing effect of a flat plate with embedded microgrooves. In addition, the Navier-Stokes transport equations describing the fluid motion are particularized for incompressible flows, and the turbulence quantities are evaluated using the linear pressure-strain Reynolds stress transport (RST) model of Gibson and Launder (1978). This choice of a turbulence model is explained as effects such as the anisotropy of the Reynolds stresses due to strong swirling motion, streamline curvature, and rapid changes in strain-rate and secondary flows are accounted for. The fluid motion, and the turbulence quantities are estimated by the Finite-Volume method, and the results are presented and discussed in terms of the state of turbulence.

2. MATHEMATICAL MODEL

2.1 Conservation equations

The incompressible flow, unsteady state Navier-Stokes transport equations for continuity and momentum, equations (1) and (2) respectively, are used to compute the fluid motion under the assumptions there are no adverse pressure gradients and the gravitational effects are unimportant:

$$\frac{d}{dt}\int_V dV + \oint_A \mathbf{u}\cdot\mathbf{da} = 0 \text{ , and} \tag{1}$$

$$\frac{d}{dt}\int_V \mathbf{u}dV + \oint_A \mathbf{u}\otimes\mathbf{u}\cdot\mathbf{da} = 1/\rho\oint_A \mathbf{T}\cdot\mathbf{da} \text{ .} \tag{2}$$

In the preceding equations, ρ is the density, $\mathbf{da}$ is an infinitesimal area vector, dV is an infinitesimal volume, and $\mathbf{u}$ is the velocity vector. In the left-hand side of Eq. (2) are the transient and the advective flux terms, and in the right-hand side is the viscous flux term, where the viscous stress tensor $\mathbf{T} = \mathbf{T}_l + \mathbf{T}_t$ is the sum of the laminar and turbulent stress tensors respectively. The laminar stress tensor is given by

$$\mathbf{T}_l = \mu[\nabla\mathbf{u} + \nabla\mathbf{u}^{\mathrm{T}} - 2/3\,(\nabla\cdot\mathbf{u})\mathbf{I}] \text{ ,} \tag{3}$$

where μ is the viscosity, and $\mathbf{I}$ is the identity tensor. The turbulent stress tensor $\mathbf{T}_t$, and other turbulent quantities are computed with the transport equations of the linear pressure-strain RST turbulence model (later detailed).

2.2 The state of turbulence

One can examine the anisotropy of the Reynolds stresses through the normalized anisotropy tensor $\mathbf{B}$, defined by its components as

$$B_{ij} \equiv \overline{u_i'u_j'}/\overline{u_k'u_k'} - 1/3\delta_{ij} = A_{ij}/2k \text{ .} \tag{4}$$

Tensor $\mathbf{B}$ has zero trace (i.e., $\mathrm{I}_{\mathbf{B}} \equiv tr(\mathbf{B}) = B_{ii} = 0$), and consequently it has just two independent variants, $\mathrm{II}_{\mathbf{B}} \equiv 1/2[-\mathrm{tr}(\mathbf{B}^2)]$ and $\mathrm{III}_{\mathbf{B}} \equiv \det(\mathbf{B})$. By setting $6\eta^2 = -2\mathrm{II}_{\mathbf{B}}$ and $6\xi^3 = 3\mathrm{III}_{\mathbf{B}}$, the state of the anisotropy can be determined in terms of ξ and η at any point and time in a turbulent flow, and the result plotted in the ξ-η plane. The special states of the Reynolds-stress tensor correspond to particular points in that plane, herein called the Lumley-Pope triangle (Lumley, 1978; Pope, 2000). Every Reynolds-stress that can occur in a turbulent flow has a matching point inside the Lumley-Pope triangle, and outside points correspond to Reynolds stresses having negative or complex eigenvalues (i.e., non-realizable turbulence). The isotropic state of turbulence corresponds to the point where $\xi = \eta = 0$. The two-component, axisymmetric state occurs when $\xi = -1/6$ and $\eta = 1/6$. The axisymmetric state of turbulence occurs when $\xi = \eta$ ($\mathbf{B}$ has one large eigenvalue) or $\xi = -\eta$ ($\mathbf{B}$ has one small eigenvalue), and the two-component state of turbulence is characterized by the situation where $\eta = (1/27 + 2\xi^3)^{1/3}$. In order to increase the near-wall anisotropy, i.e., to influence the state of the turbulence towards the one-component state, either one of the velocity fluctuations should be amplified or one of them should be damped. Therefore, surface designs exploring the larger streamwise fluctuations while kinematically restricting the tangential ones should attain the desired drag-reducing effect.

2.3 The drag reduction model

The strategy to detect the drag reducing effect of the microgrooves is to compare the drag force D of a flow past a microgrooved surface with that past a smooth surface of the same wetted area A_w, while keeping the similarity of the flows. In addition, the product ρV (i.e., the mass of fluid inside the control volume V at any time) is kept constant to make sure that any differences in the computed values of the average specific energy dissipation rate

$$\bar{E} = A_w \tau_w \bar{U}_B / \rho V \tag{5}$$

are due to the influence of the microgrooves on the product $\tau_w \bar{U}_B$, where $\bar{U}_B = 1/A \int_A U dA$ is the bulk velocity of the flow leaving the computational domain through a pressure-boundary of area A. With this purpose, the geometry of a flat plate with microgrooves is presented in Fig. 3, where one may observe that the flat plate length is L, and its width is W. The height of the microgrooves is c, and their width is a. In addition, the microgrooves are separated by a distance b, and the total width of the grooved surface is W_g. The grooved surface begins at a streamwise distance L_{off} from the leading edge, which is located at $x = 0$ m. The distance L_{crit} characterizes the region where the flow is laminar or transitional, and $L' > L$ is the length of a smooth flat that has the same width and wetted area of the grooved flat plate being compared.

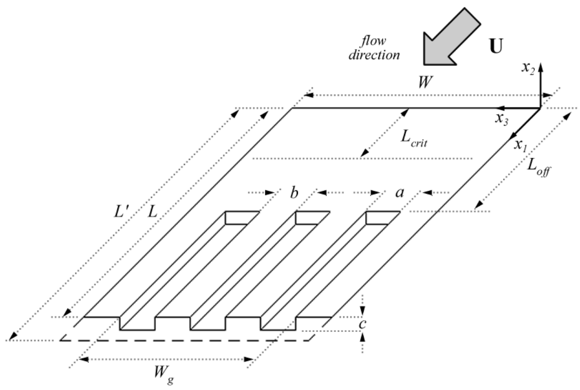

Figure 3. Geometry and feature lines of a flat plate with microgrooves (not in scale)

The choice of increasing the length of the smooth flat plate to maintain the same wetted area (as opposed to increasing its width) aims to preserve the grid node distribution in the cross-flow direction. Moreover, the shear stresses can be integrated with respect to any streamwise distance, thus allowing the grooved and smooth models to be easily compared for the same local Reynolds number. The increased length causes the volume of the computational domain to grow, and this side-effect is neutralized by reducing the height of the domain such that the product ρV in Eq. (5) is kept constant.

The drag reduction DR is given by

$$DR = 1 - D_g / D_s \,, \tag{6}$$

where D_g and D_s are the drag forces exerted by the flow past a flat plate with grooved and smooth surface respectively. In Eq. (6),

$$D_g = (1/2)\rho U_\infty^2 \{C_D(L)[(W - W_g)L + W_g L_{off} + (n-1)b(L - L_{off})] + c_{f,g} n A_g\}, \text{ and} \tag{7}$$

$$D_s = C_D(L')(1/2)\rho U_\infty^2 W L' \,. \tag{8}$$

In Eq. (7), the terms in the square brackets are the contribution to the total drag of the surfaces exposed to turbulent flow, and the second term represents the contribution of the n grooves of wetted area A_g. According to Schlichting (1979), one may obtain the turbulent drag coefficient C_D as a function of the local Reynolds number Re_x with

$$C_D(Re_x) = 0.455/(\log Re_x)^{2.58} - A(x)/Re_x, \text{ where} \tag{9}$$

$$A(Re_x) = Re_{L_{crit}}(0.074 Re_x^{-1/5} - 1.328 Re_x^{1/2}) \,, \tag{10}$$

$Re_x \equiv \rho U_\infty x / \mu$, and $x = \{L, L'\}$. Under the assumptions the grooves are completely immersed in the viscous sublayer, the flow is incompressible and steady (not accelerated), there are no mean motion in the x_2 and x_3 directions, and in the absence of an adverse pressure gradient and gravitational forces, the Navier-Stokes conservation equations applied to the flow inside the grooves reduce to the Laplace equation $\nabla^2 \overline{u_1} = 0$ and $\partial \overline{u_1} / \partial x_1 = 0$. A solution for that pair of equations is the plane Couette flow, being such fact explored by Bechert and Bartenwerfer (1989) to compute viscous flows past ribbed surfaces, and by Luchini et al. (1991) to evaluate the resistance of a grooved surface to parallel and cross flows. In the plane Couette flow, the skin friction coefficient in Eq. (7) is given by

$$c_{f,g} = 2/Re_g \ , \tag{11}$$

where Re_g is the Reynolds number that characterizes the flow inside the grooves, evaluated as

$$Re_g = u_g R_h/\nu \ . \tag{12}$$

In Eq. (12), u_g is the characteristic velocity inside the grooves in the x_1 direction, and $R_h = A_{g,cross}/p_{g,wet}$ is the hydraulic radius of the groove (obtained by dividing the groove cross-section by its wetted perimeter). The value of u_g is related to the flow velocity in the vicinity of the grooves. Assuming the reference velocity of the flow outside the grooves to be the closest approximation, one can obtain that velocity with

$$u_g \cong u_* = U(C_D(L)/2)^{1/2} \ . \tag{13}$$

The groove wetted area evaluates as

$$A_g = (L - L_{off})p_{g,wet} \ , \tag{14}$$

where $A_{g,cross}$ and $p_{g,wet}$ depend on the groove topology.

The maximum drag reduction is obtained by setting $Re_L \to \infty$. In this situation, the drag contribution of the grooves tends to vanish as $c_{f,g} \to 0$, thus reducing Eq. (7) to

$$DR_{max} = 1 - \left[(W - W_g)L/WL' + W_g L_{off}/WL' + (n-1)b(L - L_{off})/WL'\right]. \tag{15}$$

Equation (15) shows that the maximum drag reduction depends on geometrical parameters only. One should notice that in equations (7) and (8), setting $L = L'$ would cause the drag to be compared between surfaces of same projected area, as opposed to comparing to the same wetted area.

2.4 The linear pressure-strain RST turbulence model

In the linear pressure-strain RST turbulence model of Gibson and Launder (1978), the turbulent stress is defined as

$$\mathbf{T}_t \equiv -\rho\mathbf{R} \ , \tag{16}$$

where $\mathbf{R} \equiv R_{ij} = \overline{u_i' u_j'}$ is the Reynolds stress tensor. The diagonal components of $\mathbf{R}$ ($\overline{u_1'^2}$, $\overline{u_2'^2}$, and $\overline{u_3'^2}$ in the streamwise, normal, and tangential directions respectively) are normal stresses, while the off-diagonal components (e.g. $\overline{u_1' u_2'}$) are shear stresses. The transport equation of the Reynolds stress tensor is

$$\frac{d}{dt}\int_V \mathbf{R}dV + \int_A \mathbf{R}(\mathbf{u}\cdot\mathbf{da}) = 1/\rho\left[\int_A \mathbf{D}\cdot\mathbf{da} + \int_V(\mathbf{P} - 2/3\,\rho\mathbf{I}\varepsilon + \mathbf{\Phi})dV\right] , \tag{17}$$

where the tensor terms in the right-hand side are the turbulent diffusion, turbulent production, isotropic turbulent dissipation rate, and linear pressure-strain. The turbulent diffusion term is computed with

$$\mathbf{D} = (\mu + \mu_t/\sigma_k)\nabla\mathbf{R} \ , \tag{18}$$

where the isotropic turbulent viscosity μ_t is given by

$$\mu_t = \rho C_\mu k^2/\varepsilon \ . \tag{19}$$

In the previous equations, $\sigma_k = 0.82$ and $C_\mu = 0.09$ are model coefficients. The turbulent kinetic energy k is obtained directly from the Reynolds stress tensor, and it is defined as

$$k \equiv 1/2\,(tr\ \mathbf{R}) \ . \tag{20}$$

The isotropic turbulent dissipation rate ε is obtained from the transport equation

$$\frac{d}{dt}\int_V \varepsilon dV + \int_A \varepsilon\mathbf{u}\cdot\mathbf{da} = 1/\rho\left[\int_A(\mu + \mu_t/\sigma_\varepsilon)\nabla\varepsilon\cdot\mathbf{da} + \int_V[\varepsilon/k\,(C_{\varepsilon 1} tr\ \mathbf{P} - C_{\varepsilon 2}\rho\varepsilon)]dV\right] . \tag{21}$$

In the above equation, $C_{\varepsilon 1} = 1.44$, $C_{\varepsilon 2} = 1.92$, and $\sigma_\varepsilon = 1.0$ are model coefficients, and the turbulent production tensor is evaluated without recourse to modeling as

$$\mathbf{P} = -\rho(\mathbf{R} \cdot \nabla\mathbf{u}^{\mathrm{T}} + \nabla\mathbf{u} \cdot \mathbf{R}) \ . \tag{22}$$

The pressure-strain interactions affect the Reynolds stresses by two different physical processes - first due to pressure fluctuations due to the mutual interaction between turbulent scales and second, the interaction between these regions and those with different average speeds (Launder et al., 1975). In Eq. (17), those interactions are accounted for by the linear pressure-strain tensor term given by

$$\mathbf{\Phi} = \mathbf{\Phi}_s + \mathbf{\Phi}_r + \mathbf{\Phi}_{1w} + \mathbf{\Phi}_{2w} \ , \tag{23}$$

where the four terms are the slow part, the rapid part and their respective wall-reflection terms. The formulation of the terms of Eq. (23) can be found in Rodi, 1991.

2.5 Near-wall treatment

The turbulent kinetic energy is computed with Eq. (20) throughout the domain and down right to the wall, and the near-wall values of the turbulent viscosity and turbulent dissipation rate merge with their respective isotropic values, obtained with Eq. (19) and (21) respectively, by means of a one-equation blending function. In this two-layer approach to solving turbulent quantities (Rodi, 1991), the near-wall turbulent dissipation rate is given by

$$\varepsilon_{wall} = k^{3/2}/l_\varepsilon \ , \tag{24}$$

where l_ε is a length-scale that is computed following the proposition of Wolfstein (1969):

$$l_\varepsilon = c_l y[1 - exp(-Re_y/A_\varepsilon)] \ . \tag{25}$$

In the above equation, $Re_y \equiv \rho\sqrt{k}y/\mu$, $A_\varepsilon = 2c_l$ and $c_l = \kappa C_\mu^{-3/4}$are model coefficients, and $\kappa = 0.42$ is the Kolmogorov constant. The near-wall viscosity is computed with

$$\mu_{t,wall} = \lambda\mu_t + (1-\lambda)\mu(\mu_t/\mu)_{wall} \ , \tag{26}$$

where λ is a blending factor, and $(\mu_t/\mu)_{wall}$ is the near-wall turbulent viscosity ratio which is given by the equation

$$(\mu_t/\mu)_{wall} = Re_y C_\mu^{1/4}\kappa[1 - exp(-Re_y/A_\mu)] \ . \tag{27}$$

The blending factor λ is computed with

$$\lambda = 1/2\{1 + tanh[(Re_y - Re_y^*)/A]\} \ , \tag{28}$$

and in the previous equations, $A_\mu = 70$, $Re_y^* = 60$ and $A = 4.35$ are model coefficients.

3. NUMERICAL METHOD

3.1 The Finite-Volume method

The Finite-Volume method (Patankar, 1980) is adopted to approximate the transport equations of the mathematical model. This approximation approach results in the linear system

$$\mathbf{Ax} = \mathbf{b} \tag{29}$$

which represents the algebraic equations for each cell of the grid. Matrix **A** represents the coefficients of the linear system, vector **x** represents the unknowns, and vector **b** represents the residuals. In order to solve Eq. (29), the authors adopt the CFD code Star-CCM+ (CD-adapco, 2013), which is setup to compute the pressure-velocity coupling of the flow using the SIMPLE algorithm (Patankar and Spalding, 1972), being the iteration scheme the Gauss-Seidel with under-relaxation of velocity, pressure, and turbulent viscosity quantities.

3.2 Assessment of the numerical uncertainty

The estimation of the numerical uncertainty and grid independence of the results follows the generalized Richardson's Extrapolation Method (Roache, 1998). In this method, the asymptotic value ϕ_0 of a scalar ϕ is given by

$$\phi_0 \cong \phi_1 + (\phi_1 - \phi_2)/(r_{12}^{p_{obs}} - 1)\,, \tag{30}$$

where ϕ_1 and ϕ_2 are the values computed with the fine and coarse grids respectively, r_{12} is the refinement ratio between those grids, and p_{obs} is the observed order of convergence of the grid set. The refinement ratio r_{12} is given by

$$r_{12} = \ [(\text{fine grid cells})\ /(\text{coarse grid cells})]^{1/3}\,, \tag{31}$$

and the observed order of convergence is obtained by solving iteratively for p_{obs} the equation

$$\epsilon_{23}\%/(r_{23}^{p_{obs}} - 1) = r_{12}^{p_{obs}}[\epsilon_{12}\%/(r_{12}^{p_{obs}} - 1)]\,, \tag{32}$$

where the subscript "3" refers to the coarsest grid. In the previous equation, the Richardson Error Estimator is computed with

$$\epsilon_{\mathrm{n,\,n\text{-}1}}\% = 100(\phi_{\mathrm{n}} - \phi_{\mathrm{n\text{-}1}})/\phi_{\mathrm{n\text{-}1}}\,, \tag{33}$$

where n={1,2,3}. The grid convergence index of the fine grid is calculated with

$$GCI_{12}\% = F_S|\epsilon_{12}\%|/(r_{12}^{p_{obs}} - 1)\,, \tag{34}$$

where $F_S = 1.25$ is as a factor of safety over those quantities. The asymptotic value ϕ_0 is considered to be grid independent when $\alpha/r_{12}^{p_{obs}} \approx 1$, where $\alpha = GCI_{23}\%/GCI_{12}\%$.

3.3 Computational domain, grid generation and boundary conditions

The computational domain has prismatic topology, and it is delimited by the flat plate outline and extends to a height H from the flat plate surface. The domain is discretized with hexahedral cells, layered according to a one-parameter hyperbolic tangent stretching function (Vinokur, 1980).

$$h_i = 1 + tanh[r_h i/(N - 1)]/tanh(r_h)\,, \tag{35}$$

where h_i is the height of the i-nth cell layer, r_h is the stretching factor of the cell layers, and $N > 1$ is the number of cell layers. The design of the grids follows well-known guidelines (Mavriplis et. al, 2009) which recommend three refinement levels for verification and numerical uncertainty analysis; two equally spaced cell layers adjacent to the walls; $r_h \leq 1.25$; design grid refinement ratio $r_{ref} \cong \sqrt[3]{3}$; dimensionless near-wall distance $y_w^+ \equiv \rho h_0 u_*/\mu \cong 1$, where h_0 is the height of the cell layer adjacent to the wall, $u_* = \sqrt{\tau_w/\rho}$ is the reference velocity, and τ_w is the wall shear-stress. The design value of y_w^+ dictates the height h_0 of the cell layer adjacent to the wall with

$$h_0 = 5.1988 y_w^+ L Re_L^{-0.9}\,, \tag{36}$$

(Schlichting, 1979), where L is the characteristic length, and $Re_L \equiv \rho U_\infty L/\mu$ is the Reynolds number. The number of cell layers spanning the turbulent boundary layer evaluates with

$$N_{B.L.} = \mathrm{int}\{\ln[\delta_{B.L.}/h_0\,(r_h - 1) + 1]/\ln(r_h)\}\,, \tag{37}$$

where $\delta_{B.L.} = 0.37 L Re_L^{-0.2}$ is the estimated thickness of the turbulent boundary layer (Schlichting, 1979). The characteristic Reynolds number of the flow past a flat plate with $L = 1.5$ m is set to $Re_L = 5\mathrm{E}6$, yielding $U_\infty = 52.2197$ m/s and Mach number $M \equiv c/U_\infty = 0.15$ (where c is the speed of sound in the air); the density $\rho = 1.1841$ kg/m^3, and the viscosity $\mu = 1.8550\mathrm{E}{-5}$ Pa·s are evaluated at the temperature $T = 300$ K. The critical Reynolds number is set to $Re_{crit} = 3.75E5$, yielding $L_{crit} = 0.1125$ m. The offset distance of the grooves from the leading edge is set to $L_{off} = 0.225$ m. The design of the microgrooves essentially aims to place them within the viscous sublayer. With this purpose, the viscous distance is evaluated as

$$\delta = 2\nu/u_g\,, \tag{38}$$

and it is used to estimate the design width a and the height c of the grooves such that their respective dimensionless values $a^+ \equiv a/\delta$ and $c^+ \equiv c/\delta$ are approximately 5. The distance b between grooves determines the groove density, i.e., W_g in Fig. (3). By selecting $n = 13$, and grooves with rectangular cross section (U-shape) having $a = 1.25\text{E-}4$ m, $c = 1\text{E-}4$ m, and $b = 3.75\text{E-}4$ m ($a^+ = 8.5$, $c^+ = 6.8$ and $b^+ = 25.4$ respectively), the drag reduction per Eq. (6) may be plotted against Re_L as shown in Fig. 4. One may observe in this plot that the drag reduction evolves from negative values for $Re_L < 1.7\text{E6}$, and up to $DR_{max} \approx 7$ % as $Re_L \to \infty$. The estimated drag reduction for $Re_L = 5\text{E6}$ is 4.3%, and in the special case where $W_g \approx W$, DR_{max} approaches 25%.

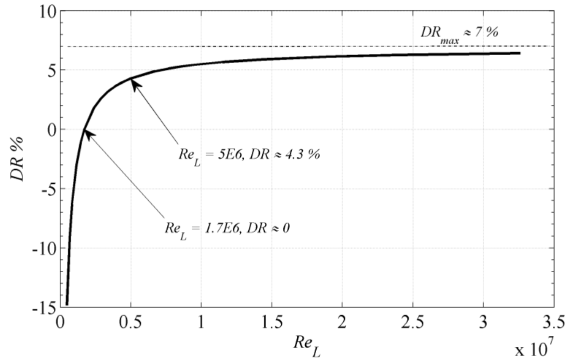

Figure 4. Drag reduction (%) versus Re_L

3.4 Boundary conditions

The boundaries of the computational domain are represented in Fig. 5, where the flow enters the domain in the normal direction of the velocity inlet boundary with uniform speed $U_\infty = 52.2197$ m/s. The flow exits the domain through the pressure-top and pressure-outlet boundaries, where the static pressure is $p_\infty = 101325$ Pa. The flat plate is modeled as a hydraulically smooth and impermeable wall. In order to prescribe the region where the flow transitions to the turbulent state, the turbulence is suppressed where $0 \le x_1 < L_{crit} = 0.1125$ m by setting to zero the turbulent viscosity, the Reynolds stresses, and the production terms in the turbulence transport equations. The microgrooved region initiates at $x_1 \ge L_{off} = 0.225$ m. The side boundaries are symmetry planes, where the shear-stress is set to zero, and the cell-face values of velocity and pressure are extrapolated from the adjacent interior cells. In all boundaries (except in the symmetry planes), the turbulence intensity is set to 0.01, and the turbulent viscosity ratio is set to 10. The initial conditions are the same as the boundary conditions.

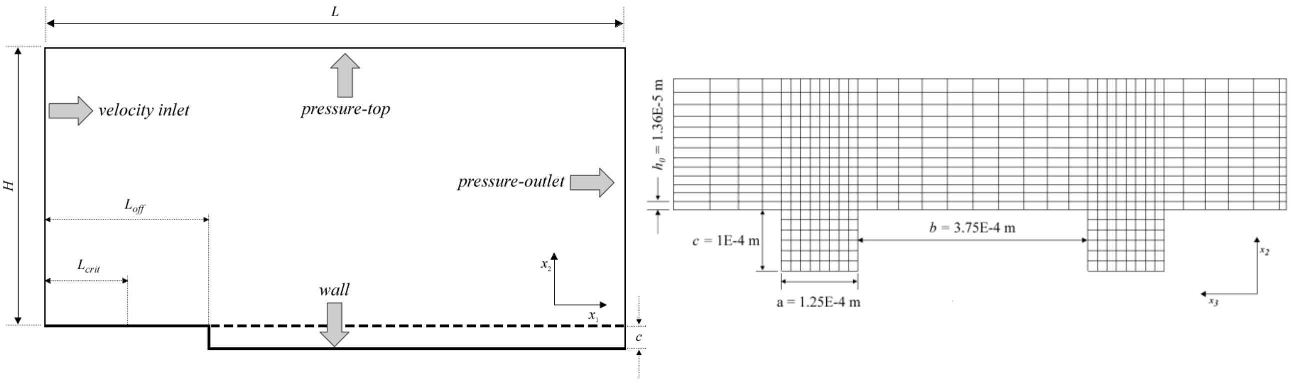

Figure 5. The boundaries of the computational domain (cross-section), and the grid in the neighborhood of the central microgrooves (not in scale)

4. RESULTS AND DISCUSSION

4.1 Grid verification and numerical uncertainty analysis

The smooth and grooved grids are verified following the methodology previously described. To this end, the computed drag force magnitude replaces the scalar ϕ in Eq. (30). The drag force is given by

$$D = \sum_f [(p_f - p_\infty)\mathbf{a}_f - \mathbf{T}_f \cdot \mathbf{a}_f] \cdot \mathbf{i}\,, \tag{39}$$

where p_f is a cell-face pressure, $\mathbf{a}_f$ is a cell-face area vector, p_∞ is the reference pressure, $\mathbf{T}_f$ is the stress tensor at a cell-face f, and $\mathbf{i}$ is the unit vector in the x_1 direction. The verification results are presented in Tab. 2, where the $\alpha/r_{12}^{p_{obs}}$ values approximating the unity indicate the results to be grid independent, and within a maximum error band of 0.05% centered on the asymptotic value. Also, the $\Delta\,\%$ values do not significantly change with grid refinement, further indicating the grids are in the asymptotic convergence region. Additionally, the decrease of the turbulent contribution $D_{1,turb}$ to the total drag force D_1 accounts for most of the drag reduction effect, being the drag influence of the laminar region $D_{1,lam}$ numerically negligible and nearly the same for both models (such fact indicating the effectiveness of the turbulence suppression in the region of the flow where $L < L_{crit}$). Further, the bulk velocity of the smooth model decreased, and the average specific energy dissipation rate increased, signifying that the smooth model dissipates more energy than a grooved model with the same wetted area and inbound mass rate. The values of D_g evaluated at $Re_L =$ 5.0E6, whilst the values of D_s evaluated at $Re_{L'} = 5.2\text{E}6$ in order to keep the wetted area A_w and the product ρV constant in Eq. (5) when computing the average specific energy dissipation rate.

Table 2. Verification of the numerical uncertainty and grid independence of the results

Eq. (60)	D_1*	D_2	D_3	ϵ_{23}%	ϵ_{12}%	p_{obs}	D_0	GCI_{23}%	GCI_{12}%	$\alpha/r_{12}^{p_{obs}}$
D_g	3.8167E-1	3.8177E-1	3.8219E-1	1.0958E-3	2.6445E-4	4.8630	3.8161E-1	0.0500	0.0169	1.0000
D_s	3.9642E-1	3.9646E-1	3.9685E-1	1.0002E-3	1.0433E-4	7.4843	3.9641E-1	0.0160	0.0029	1.0000
Δ %	3.7208	3.7054	3.6962				3.7316			

D_1*	D_g	D_s	Δ %
D	3.8167E-1	3.9642E-1	3.7208
D_{lam}	2.0955E-2	2.0955E-2	0.0003
D_{turb}	3.6071E-1	3.7546E-1	3.9284
$\bar{U}_B$	5.1890E+1	5.1855E+1	-0.0674
$\bar{E}$	5.9465E+2	6.1722E+2	3.6559

4.2 Validation of the numerical method

The numerical method is validated by comparing the computed drag coefficient for the fine grid of the smooth model ($C_{D,1}$), against the theoretical value $C_D(Re_x)$ obtained with Eq. (9) by setting $Re_x = 5.2\text{E}6$. As one may observe in Tab. 3, the difference between those values is less than 0.2 %, and the drag reduction estimated by Eq. (6) remarkably matches the computed and the theoretical values.

Table 3. Validation Results

	Grooved	Smooth	Δ %
$C_{D,1}$, $Re_L = 5.2\text{E}6$		3.1352E-3	
C_D, $Re_x = 5.2\text{E}6$, Eq. (6)		3.1410E-3	
Δ %		**0.18**	
	C_D		
$C_{D,1}$, $Re_L = 5.0\text{E}6$	3.0185E-3	3.1515E-3	**4.22**
DR (%), Eq. (6)			**4.28**

In addition to validating the numerical method against well-known analytical results for the smooth flat plate, a microgrooved channel flow (Moser et al., 1999) is also examined for $Re_\tau = 187$, $n = 34$, $a^+ = 5$, $b^+ = 14$, and $c^+ = 5$. The DNS results of Frohnapfel (2007) indicate $DR = 18\%$, and the result obtained by applying the numerical method is $DR = 16\%$ with $GCI_{12}\% = 0.17$. Such result indicates the validity of the numerical method, and the transfer of flow control into the RST turbulence model. However, the authors emphasize that the transfer of flow control into RANS based models has been debated, and it is to some extent controversial (Frohnapfel, 2015).

4.3 Assessment of the shear stresses

The drag-reducing effect of the microgrooves can also be validated by comparing the shear stresses inside and outside the microgrooves. With this purpose, in figures 6a and 6b the magnitude of the tangential and streamwise shear stresses respectively, are compared alongside the lines that define the axis of the central groove, and the line at $x_3 =$ 0.0125 m where the surface is smooth and sufficiently away from the grooved region. The spikes in these plots indicate the regions of the flow where the transition from the laminar to the turbulent state occurs ($L \sim L_{crit}$), and where the grooved region begins ($L \sim L_{off}$). In Fig. 6a, one can observe the tangential stresses being nearly zero where the surface is smooth. However, in the grooved region the tangential shear stresses spike up, and then sharply drop by almost one order of magnitude where $L \sim L_{off}$. Although the tangential stress continuously increases with the Reynolds number inside the groove, it remains less than that of the flat plate with smooth surface. The streamwise stresses are plotted in

Fig. 6b, where the transition of the flow from laminar to the turbulent state can be easily identified by the peak in the shear stress immediately after $Re_{L_{crit}}$. The shear stress sharply decreases as the flow ingresses the groove, and the reduction is approximately 2∼3 orders of magnitude higher than that of the tangential stress.

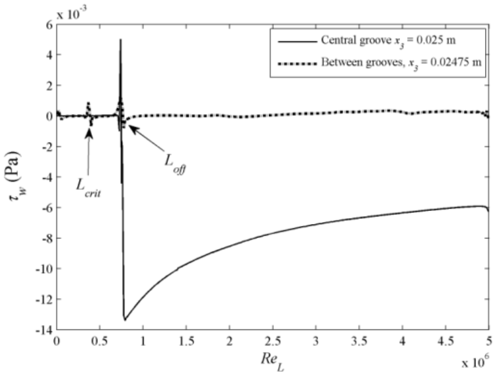

Figure 6a. Magnitude of the tangential shear stress

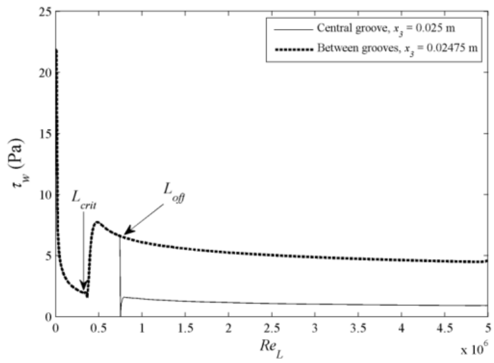

Figure 6c. Magnitude of the streamwise shear stress

4.4 The state of turbulence and the anisotropy of the Reynolds Stresses

The anisotropy of the Reynolds stresses can be conveniently examined by mapping the values of η in the region near the central grooves that extends in the normal direction up to $y^+ \approx 600$. With this purpose, Fig. 7 displays the partial cross-section of the microgrooved flat plate, where $Re_{x_1} \approx 4.8E6$ ($x_1 = 1.45$ m).

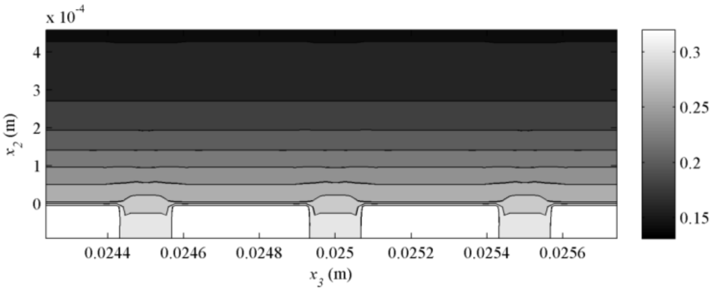

Figure 7. Mapping of the anisotropy η in the region near the central groove

The highest anisotropy is found in the interior of the grooves, therefore indicating the state of turbulence as being one-component (i.e., $\eta \approx 1/3$) in those regions. Outside the grooves, the turbulence departs from the one-component state and begins to evolve towards the isotropy, and alongside the line that bounds the axisymmetric contraction in the Lumley-Pope triangle represented in Fig. 8a. In Fig. 8b, the Lumley-Pope triangle is plotted for the region between two consecutive grooves, and one may observe that for the same y^+ the state of turbulence is less anisotropic, and the maximum value of η is smaller than that of inside the grooved regions.

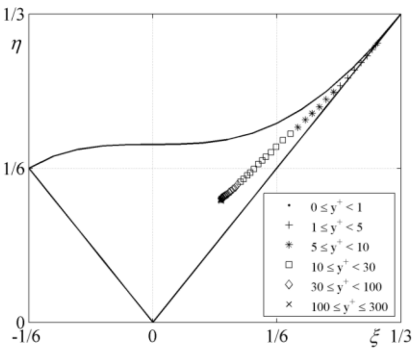

Figure 8a. The state of turbulence inside the central groove ($x_3 = 0.025$ m)

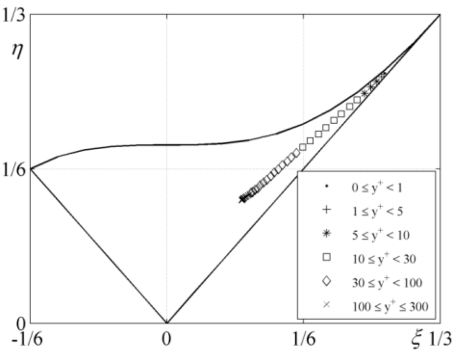

Figure 8b. The state of turbulence between grooves ($x_3 = 0.02475$ m)

4.5 The behavior of the Reynolds Stresses

The behavior of the Reynolds stresses in the regions inside and between grooves are investigated to establishing a parallel with a channel flow. In Fig. 9a, the streamwise, tangential, and normal dimensionless Reynolds stresses inside the central grove are plotted. In Fig. 9b, that plot is detailed where $y^+ < 15$, and one can observe that the normal and tangential stresses display the same gradient, and that the streamwise Reynolds stress component predominates, being such fact explained by the absence of the two-component turbulence state inside the grooves.

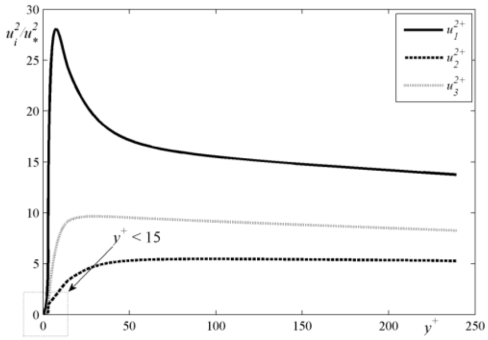

Figure 9a. Dimensionless streamwise, tangential, and normal Reynolds stresses inside the central groove

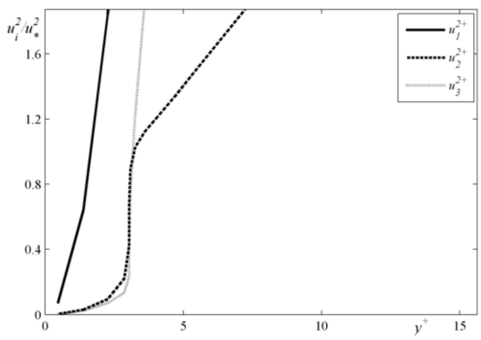

Figure 9b. Detail of the dimensionless streamwise, tangential, and normal Reynolds stresses inside the central groove

5. CONCLUSIONS

The use of microgrooved surfaces as a passive flow control strategy to reducing the turbulence drag was discussed, and the results in the literature indicated that moderate gains can be achieved by using microgrooves in channel flows. In this work, the authors investigated the hypothesis that such arrangement of microgrooves could also reduce the turbulence drag of flows past a flat plate. With this purpose, the drag-reducing effect was associated with the state of turbulence, and a model to estimating the potential in drag reduction was introduced. That model predicts the drag reduction as depending solely on the flow and geometry settings. Moreover, the maximum drag reduction asymptotically approaches a limit which is determined by the topology of the grooves. The unsteady, incompressible formulation of the Navier-Stokes conservation equations, the linear pressure-strain Reynolds Stress Transport turbulence model, and the Finite-Volume method modeled the flows. After verifying and validating the results, an assessment of the state of turbulence and the anisotropy of the Reynolds stresses confirmed the prevalence of the one-component state inside the microgrooves, and the achievement of a drag-reducing effect matching the predictions of the proposed model.

6. ACKNOWLEDGEMENTS

The authors thank the financial support from CAPES through a post-doctorate scholarship grant for Beck, P.A, and from CNPq through scientific productivity grants for Vielmo, H.A.

7. REFERENCES

Bechert, D.W, and Bartenwerfer, M., 1989. “The viscous flow on surfaces with longitudinal ribs”. *J. Fluid Mech*. Vol. 206, pp. 105-129.
Bechert, D.W., Bruse, M., Hage, W., van der Hoeven, J.G.T., and Hoppe, G., 1997. “Experiments on drag-reducing surfaces and their optimization with an adjustable geometry”. *J. Fluid Mech.* Vol. 338, pp. 59-87.
CD-adapco, 2013. *STAR-CCM+ Version 8.06*. User’s Guide, p. 13302.
Choi, K.S., 1989. “Near-wall structures of a turbulent boundary layer with riblets”. *J. Fluid Mech*. Vol. 208, pp. 417-458.
Choi, H., Moin, P., and Kim, J., 1992. “Turbulent drag reduction: studies of feedback control and flow over riblets”. *Report No. TF-55*. Department of Mechanical Engineering, Stanford University.
European Commission, 2011. “Flightpath 2050 - Europe‘s Vision for Aviation”, *Report of the High Level Group on Aviation Research*.
Frohnapfel, B., 2007. “Flow control of near-wall turbulence”. *PhD thesis*. University of Erlangen-Nuremberg, Shaker Verlag, Aachen.
Frohnapfel, B., Jovanović, J., and Delgado, A., 2007. “Experimental Investigations of Turbulent Drag Reduction by Surface-Embedded Grooves”. *J. Fluid Mech*. Vol. 590, pp. 107–116.
Frohnapfel, B., 2015. *Private communications*.

Gibson, M.M. and Launder, B.E., 1978. “Ground effects on pressure fluctuations in the atmospheric boundary layer”. *J. Fluid Mech*. Vol. 86, pp. 491-511.

Gollub, J., 2006. “Research in fluid dynamics: meeting national needs”, *Report of the US National Committee on Theoretical and Applied Mechanics*.

Hooshmand, A., Youngs, R., Wallace, J.M., and Balint, J.L., 1983. “An experimental study of changes in the structure of a turbulent boundary layer due to surface geometry changes”. *AIAA Paper 83-0230*. Aerospace Sciences Meeting, Reno, NV.

Jovanović, J., and Hillerbrand, R., 2005. “On peculiar property of the velocity fluctuations in wall bounded flows”, *Journal of Thermal Sciences*. Vol. 9, pp. 3–12.

Jovanović, J., Pashtrapanska, M., Frohnapfel, B., Durst, F., Koskinen, and J., Koskinen, K., 2006. “On the mechanism responsible for turbulent drag reduction by dilute addition of high polymers: theory, experiments, simulations, and predictions”. *Journal of Fluids Engineering*. Vol. 128, pp. 118-130.

Launder, B.E., Reece, G.J. and Rodi, W., 1975. “Progress in the development of a Reynolds-stress turbulence closure”. *J. Fluid. Mech*. Vol. 68, pp. 537-566.

Luchini, P., Manzo, F., and Pozzi, A., 1991. “Resistance of a grooved surface to parallel flow and cross-flow”, *J. Fluid Mech.*, Vol. 228, pp. 87–109.

Lumley, J.L., 1978. “Computational Modeling of Turbulent Flows”. *Advances in Applied Mechanics*. Vol. 18, pp. 123-176.

Mavriplis, D.J., Vassberg, J.C., Tinoco, E.N., Mani, M., Brodersen, O.P., Eisfeld, B., Wahls, R.A., Morrison, J.H., Zickuhr, T., Levy, D. and Murayama M., 2009. “Grid Quality and Resolution Issues from the Drag Prediction Workshop Series”. *J. Aircraft.* Vol. 46, pp. 935-950.

Mohammadi, A., and Floryan, J. M., 2013, “Pressure losses in grooved channels”, *J. Fluid Mech*. Vol. 725, pp. 23-54

Moser, R.D., Kim, J. and Mansour, N.N., 1999. “Direct numerical simulation of turbulent channel flow up to $Re_\tau = 590$”, *Physics of Fluids*, Vol. 11, pp. 943-945.

Patankar, S.V., 1980. *Numerical Heat Transfer and Fluid Flow*. Taylor & Francis Group LLC, NY.

Patankar, S.V. and Spalding, D.B., 1972. “A Calculation Procedure for Heat, Mass and Momentum Transfer in Three-Dimensional Parabolic Flows”, *Int. J. Heat. Mass Tran.* Vol. 15, pp. 1787-1806.

Pope, S.B., 2000. *Turbulent Flows*. Cambridge University Press, UK.

Roache, P.J., 1998. *Verification and Validation in Computational Science and Engineering*. Hermosa Publishers, Albuquerque.

Rodi, W., 1991. “Experience with Two-Layer Models Combining the k-ε Model with a One-Equation Model Near the Wall”. In *29th Aerospace Sciences Meeting, January 7-10, Reno, NV, AIAA Paper 91-0216*.

Schlichting, H., 1979. *Boundary Layer Theory seventh ed.* McGraw-Hill Book Company, New York.

Suzuki, Y., and Kasagi, N., 1994. "Turbulent drag reduction mechanism above a riblet surface", *AIAA Journal*, Vol. 32, No. 9, pp. 1781-1790.

Thiede, P., 2001. “Aerodynamic drag reduction technologies”, *Proceedings of the CEAS/DragNet European Drag Reduction Conference, 19-21 June, Potsdam, Germany*.

Walsh, M.J., 1990. “Riblets”. In *Viscous Drag Reduction in Boundary Layers, edited by Bushnell, D.M., and Hefner, J.M. Progress in Astronautics and Aeronautics*, AIAA, Washington DC, Vol. 123, pp. 203-261.

Wolfstein, M., 1969. “The velocity and temperature distribution in one-dimensional flow with turbulence augmentation and pressure gradient”. *Int. J. Heat Mass Transfer*. Vol. 12, pp. 301-318.

Van Schwarz-Manen, A.D., Thijssen, J.H.H., Nieuwvett, C., Prasad, K.K., and Nieuwstadt, F.T.M., 1990. “The bursting process over drag reduction grooved surfaces”. *Proc. IUTAM Symp. on Structure of Turbulence and Drag Reduction*. Springer, Berlin, pp. 561-568.

Vinokur, M., 1980. “On one-dimensional stretching functions for finite-difference calculations”. *NASA Contractor Report 3313*. Scientific and Technical Information Branch, NASA, Washington, D.C.

8. RESPONSIBILITY NOTICE

The authors are the only responsible for the printed material included in this paper.